Numerical characterization of shock separation in a laboratory-scale nozzle

M. Nedjari

Laboratory of Materials and Reactive Systems,
Djillali Liabes University, 22000, Sidi Bel Abbes, Algeria.
e-mail: mohammed.nedjari@univ-sba.dz

A. Benarous

Mechanical department, Technology faculty,
Saad Dahlab University, Blida, Algeria.

A. Benazza

Laboratory of Materials and Reactive Systems,
Djillali Liabes University, 22000, Sidi Bel Abbes, Algeria.

Received 28 December 2021; accepted 17 April 2022

The purpose of this work is to perform a CFD study of the free shock separation (FSS) in an overexpanded nozzle. The original contraction profile of the nozzle was numerically replaced by a set of curves, where the overall length was identical with the test-rig. For the baseline case, the static pressure and the separation location exhibited a good agreement with the experimental measurements, provided by the DLR. The Error-function contraction profile has revealed a relative displacement of 1.38% on the separation location in the core flow direction. In this case, there was an increase in the thrust coefficient, that has been improved up to 1.7% in comparison with the baseline nozzle design.

Keywords: Overexpanded nozzle; contraction profile; shock separation; thrust coefficient; computational fluid dynamics (CFD).

DOI: https://doi.org/10.31349/RevMexFis.69.010601

1. Introduction

The supersonic nozzles find their application in several sectors of the research and industry, such as aerospace, turbomachinery and refrigeration engineering [1-3]. The area of spatial propulsion is specifically potential since the nozzle is among the vital components of a launcher. Indeed, for nozzles with high area ratio, the specific impulse is improved, allowing therefore for payload enhancement and launching cost reduction [4-5]. However, the internal supersonic flow is subjected to several instabilities as it operates under overexpanding conditions for almost all the mission steps [5]. As the flow develops within the divergent part of the nozzle, local free (FSS) or restricted (RSS) separation may occur inducing side loads, that can alter the structural integrity of the nozzle as well as launcher performances reduction [4,6].

The physics of flow separation remains not fully understood despite the abundance of experimental and numerical investigations on the effect of nozzle geometry (CV, DV, CV-DV junction) on shock separation appearance [7]. The developed models exhibited a lack of accuracy regarding the prediction of the position of separation, while they provided few analyses on the flow pattern downstream the separation zone.

Attempts to correlate between divergent geometry and flow morphology have been conducted for more than fifty years. The investigations on the method of characteristics (MOC) allowed for the prediction of the dynamic field in the kernel zone, providing also a practical way for divergent wall profile design [8].

Many authors focused on the sonic line curvature at the throat region and how it could influence the flow pattern at the nozzle exit. The investigations have concerned several European and US rocket nozzles and revealed the direct relation between the throat region flatness and the exit Mach number [9,10].

For several types of nozzle profiles, a variety of physical criteria for the prediction of the flow separation have been numerically provided and made available for the manufacturers [11]. These attempts focused on the effect of stagnation pressure of the separation appearance, without any accurate prediction of its position. To overcome these difficulties, many investigations were oriented on the convergent and/or divergent design approaches, *i.e.*, the so-called passive techniques.

The investigations have continued with an interest to the transonic region curvature, with the works of Cuffel *et al* [11]. The experimentations have revealed the existence of a limiting value for the CV-DV connecting arc radius, which allowed for a quasi-1D flow on the throat region, ensuring therefore an expansion flow without separation in the conical divergent.

Applications of passive techniques on propulsion raised with some developed novel curved shapes, discussed by Ho *et al*. on the contraction part of nozzles [13]. In their investigation, the authors have succeeded in simulating laminar and inviscid flows in simply convergent nozzles and have shown that flat profiles of velocity at the exit section could be obtained for different values of the flatness parameter. The investigation focused on the shape of the sonic line at the throat

region, while quantifying the corresponding discharge coefficient at the nozzle exit section.

Similar analyzes were carried out by Brassard *et al.* on curved convergent profiles, composed of two circular arcs [14]. The analyses revealed the importance of the inflection point position on the value of the dynamic uniformity index at the convergent exit section. No analysis has been provided on the flow pattern downstream the throat region.

The influence of the convergent design parameters on the sonic line curvature was recently investigated by Germer *et al* [15]. For the case of an inviscid flow, the authors highlighted the effects of the angle at the convergent inlet, the radius upstream and downstream the throat on the curve flatness of the Mach number distribution curve at the throat region. The study was not interested on the morphology of the expansion flow within the conical divergent.

Kumar *et al*. have investigated the flow configuration on a curved convergent based on polynomial profiles [16]. The authors were interested in the minimization of pressure losses on an inert fluid flow, using several degrees of interpolation, with no analysis or information on flow separation.

The present study deals with a numerical prediction of a free shock separation (FSS) within an overexpanded experimental nozzle. A preliminary control of the separation position by acting on the convergent curvature was discussed. Using four profiles for the design of the convergent (error function), a comparative study is performed to seek for the contraction shape that reproduces the highest thrust coefficient while keeping the shock separation as far as possible from the throat region. Favre averaged forms of the Navier-Stokes equations are numerically solved by means of a finite volume software. Turbulent viscosity transport is handled with the Spalart-Allmaras model whereas a Roe scheme is used for the convective fluxes terms.

2. Contraction design formulation

Over the years, many authors have been interested in methods of designing contractions for wind tunnels and nozzles. The present work deals with a design formulation for the convergent part, based on minimum length (MLN) techniques [13]. For inviscid and supersonic flows in a nozzle, a single function $y = f(x)$, provides the wall shape for the converging section, as:

$$f(x_{cv}) = (y_{ch}); \quad \frac{df(x_{cv})}{dx} = 0; \quad \frac{df(x_{th}=0)}{dx} = 0;$$
$$f(x_{th}=0) = 1; \quad x_{cv} = -L_{cv}. \tag{1}$$

To help ensure a planar sonic surface with a uniform velocity, several derivatives of $f(x)$ at the throat, are set equal to zero:

$$\frac{d^j f(0)}{dx^j} = 0; \qquad \frac{d^{l+1} f(0)}{dx^{l+1}} \neq 0; \quad j = 1, 2, ..., l. \tag{2}$$

With the constraints above, one seeks a function that also satisfies $df(x)/dx \leq 0$ in the $-L_{cv} < x < 0$, and suggests an error function profile, which is written as:

$$f(x) = a + b \times erf[\eta(z)], \tag{3}$$

where $a = 1$; $b = y_i^{1+\sigma} - 1/erf[\eta(-1)]$;

$$\eta = \frac{z^{l+1}}{1 + (-1)^l \times (l+1) \times z^{(l+2)}}$$

and $z = x/L_{cv}$ is a reduced axial coordinate. Accordingly, the convergent wall can be represented by the parametric curve:

$$f(z) = 1 + (-1)^{l+1} \times \frac{y_i^{1+\sigma} - 1}{erf[\frac{1}{l+2}]} \times erf\left(\frac{z^{l+1}}{1 + (-1)^l \times (l+1) \times z^{(l+2)}}\right), \tag{4}$$

where $\sigma = 0$ for planar flows and $\sigma = 1$ for axisymmetric flows. The expression above, represents a single, flexible, analytic function that defines the contraction shape, where y_{ch} and L_{cv} are the design data of the nozzle, and σ, l stand for the controlling parameters. The latter parameter controls the flatness of the wall at the throat, where the wall becomes flatter as l increases.

3. Flow equations

Within the calculation domain, the fluid is non reactive (GN2), having constant thermophysical properties (specific heat capacity, thermal conductivity). The mathematical formulation of the principles of conservation of mass, momentum and energy, associated with the physical properties for a compressible axisymmetric, viscous fluid is expressed in the following form:

$$\frac{\partial U}{\partial t} + \frac{\partial F}{\partial x} + \frac{1}{r}\frac{\partial r G(U)}{\partial r} = \frac{S(U)}{r}, \tag{5}$$

where:

$$U = \begin{pmatrix} \rho \\ \rho u_x \\ \rho u_r \\ \rho E \end{pmatrix}, \qquad F = \begin{pmatrix} \rho u_x \\ \rho u_x^2 + p + \tau_{xx} \\ \rho u_x u_r + \tau_{xr} \\ (\rho E + p + \sigma_{xx}) u_x + \tau_{rx} u_r - q_x \end{pmatrix},$$

$$S = \begin{pmatrix} 0 \\ 0 \\ S_r \\ 0 \end{pmatrix}, \quad G = \begin{pmatrix} \rho u_r \\ \rho u_x u_r + \tau_{xr} \\ \rho u_x u_r^2 + p + \sigma_{rr} \\ (\rho E + p + \sigma_{rr}) v + \tau_{xr} u_x - q_r \end{pmatrix}. \tag{6}$$

The stress and heat-transfer components are the sum of viscous and turbulent contributions. Hence, the source term for the flow is $S_r = p + \sigma_{\theta\theta}$. The thrust F generated by the rocket nozzle is the consequence of reaction force on the nozzle wall which is caused by the flow momentum. For axisymmetric

configurations, the thrust can be expressed by the formula below [17]:

$$F = \int (\rho V dA)V + \int \rho dA. \tag{7}$$

The thrust is generated by two parts of the rocket engine, namely the combustion chamber and the divergent nozzle. The important parameter for rocket design is the thrust coefficient C_F which is the contribution of the nozzle to the total thrust. It is written as follows [17]:

$$\begin{aligned} C_F &= \frac{F}{A_{th} p_{ch}} \\ &= \sqrt{\frac{2\gamma^2}{\gamma-1}\left(\frac{2}{\gamma+1}\right)^{\frac{\gamma+1}{\gamma-1}}\left[1-\left(\frac{p_e}{p_{ch}}\right)^{\frac{\gamma-1}{\gamma}}\right]} \\ &+ \frac{(p_e - p_a)}{A_{th} p_{ch}} A_e. \end{aligned} \tag{8}$$

4. Test facility and experimental data

The test data were obtained at DLR's cold flow test facility P6.2 in Lampoldshausen, Germany [18,19]. A dry gaseous nitrogen is used and stored in high pressure tanks outside the facility. The advantage of nitrogen compared to air is the absence of water vapour that tends to condense. The inert gas flows across a cylindrical settling chamber and cross-section constriction before it accelerates in a convergent- divergent nozzle to a supersonic velocity (Fig. 1), according to an operating NPR=25.25 [19,20].

5. Numerical computations

5.1. The computational domain and grid generation

The computational domain consists of half of the DLR nozzle with its real dimensions, attached to a far- field inflow "virtual box", making it possible to capture possible oblique shocks (Fig. 2). It is important to stress that the baseline simulation considers a directly replicated contour of the nozzle convergent, as it was featured in the experimental facility [18].

The nozzle inflow was filled with a structural grid containing 200×200 cells in both axial and radial directions. The turbulent boundary layer was resolved by a gradually fine mesh where $Y^+ < 1$ was ensured. On the box-nozzle interface, a conformal mesh was built with a cell coarsening in the axial direction. A mesh sensitivity analysis was performed on finer grids, and has revealed that the nozzle wall stress fluctuations did not exceed 3% (Fig. 3).

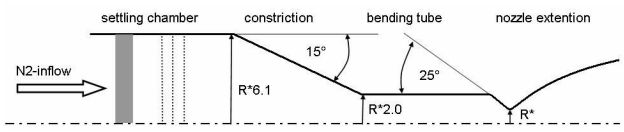

FIGURE 1. Sketch of horizontal test section of DLR P6.2 [20].

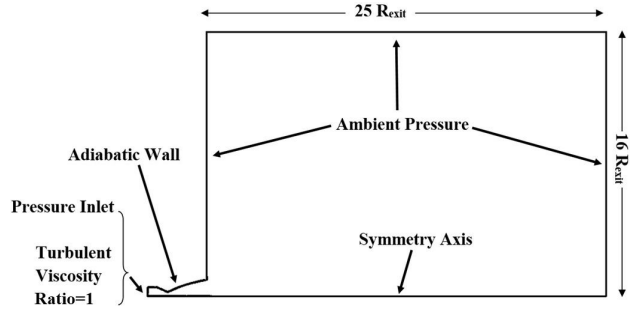

FIGURE 2. Sketch of the nozzle and the far field box with boundary conditions.

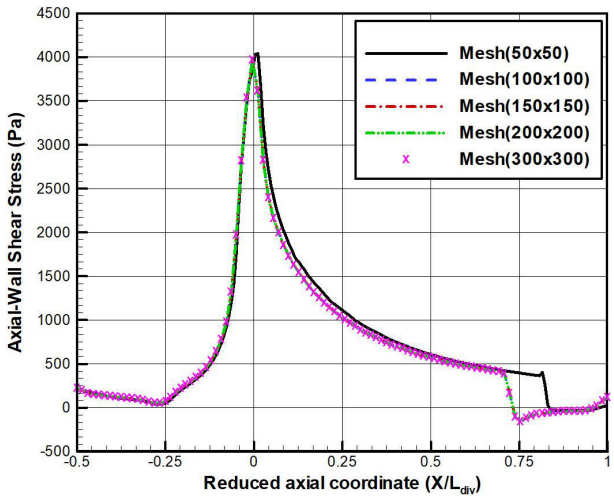

FIGURE 3. Grid refining impact on the nozzle wall stress.

5.2. Boundary conditions

As a working fluid, dry gaseous nitrogen N_2 is used, stored in high pressure tanks at 25.25 bar and 283 K. The nitrogen flow accelerates in a convergent-divergent nozzle to supersonic velocity and exits the nozzle to an ambient pressure and temperature of 1 bar and 270 K respectively. Owing to small velocities of the surrounding air, the acceleration from the ambient state to the nozzle inlet was assumed to be isentropic. Hence, Mach number, static pressure and static temperature were analytically calculated at the nozzle inlet section [21,22]. According to the experiments, the nozzle walls were considered to be adiabatic. For the outflow boundaries, all variables including static pressure were extrapolated to the ambient conditions. The nozzle centerline was treated as a symmetry axis.

5.3. Turbulence modelling

The standard turbulence model used in the simulations is the Spalart-Allmaras model [23].

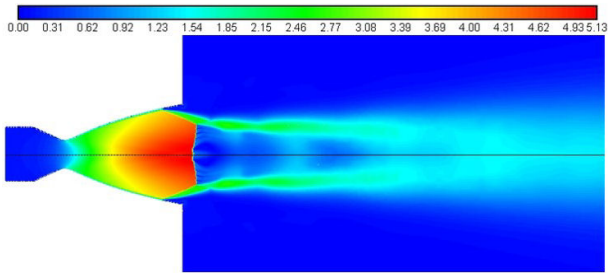

FIGURE 4. Spatial contour of the Mach number.

5.4. Discussions

The used CFD solver is based on the compressible Favre averaged Navier-Stokes equations, associated with turbulent closures. The spatial discretization is a second-order accurate both for the viscous and inviscid terms, where the latter are computed based on a Roe scheme [24].

For the nozzle geometry (baseline) used in the experimental tests [19], the numerical simulation shows a free shock separation which locates upstream of the exit section of the divergent nozzle. The flow pattern is followed by the appearance of a Mach disc downstream the separation zone (Fig. 4), which is commonly a well-known trend of an over-expanded flow.

Across the nozzle centerline, the Mach number exhibits a monotonous evolution in the convergent part of the nozzle, with a throat value $M_{th} = 0.87$ slightly lower than unity (Fig. 5). Hence, the flow at the throat region does not meet a fully sonic condition. In the downstream of the throat, the increasing of Mach number continues with a steep slope, until the exit section of the nozzle, where the predicted value $M_e = 5.13$ shows a relative underestimation of -0.39%, in comparison with the design Mach number.

The spatial contour of the axial velocity clearly shows a free shock separation (FSS) in the upstream region of the nozzle exit section (Fig. 6). The flow separation exhibits an oblique shock followed by a normal shock in the vicinity of exit section. A strong shear region is clearly depicted in the post-separation zone where an intense recirculation occurs.

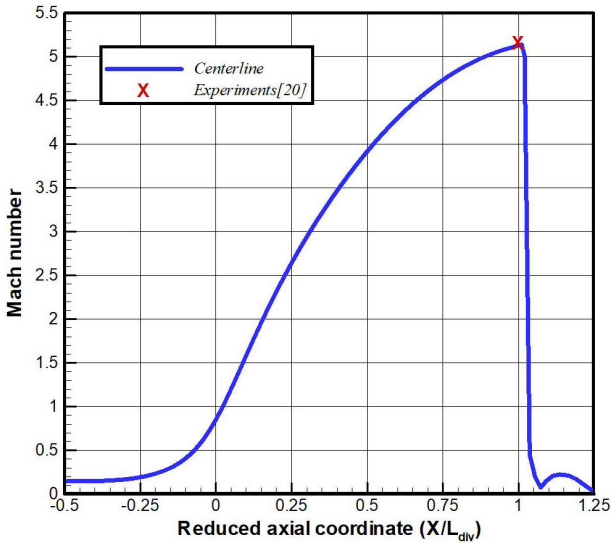

FIGURE 5. Centerline Mach number evolution.

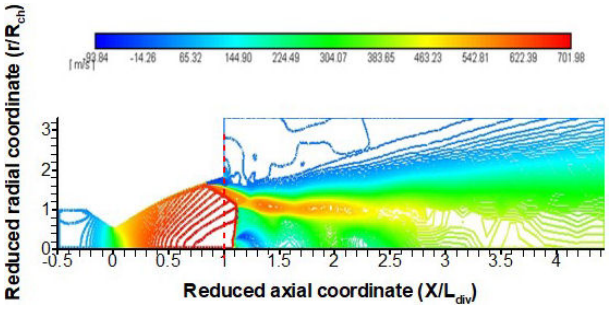

FIGURE 6. Spatial contour of the axial velocity near the separation zone.

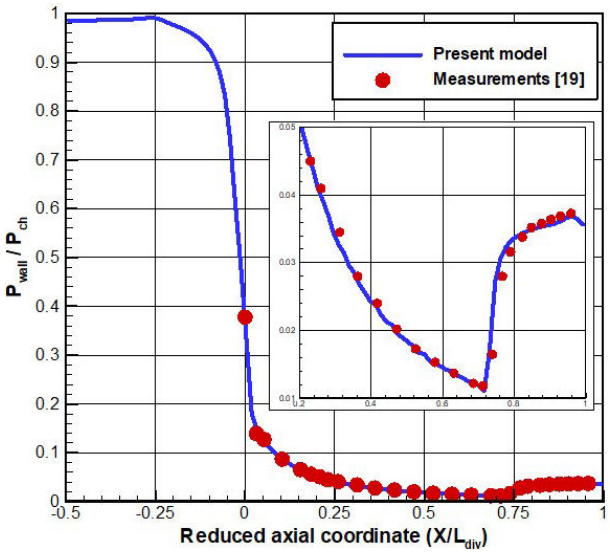

FIGURE 7. Static pressure evolution along the nozlle walls.

The evolution of the predicted wall static pressure recovers a slight recompression upstream of the nozzle exit which physically reveals a local flow separation (Fig. 7). Accordingly, the comparison between the numerical values and the local measurements on the nozzle wall is fairly satisfactory.

The location of the separation point can be predicted according to the axial wall shear stress evolution (Fig. 8). A steep decay of the corresponding curve reveals a relaxation of the boundary, which separates upstream the divergent exit. The curve reaches a zero value and becomes negative owing to the pressure gradient effects. The predicted separation location $(X/L_{\rm div} = 0.7294)$ is quite close to the experimental value, with a relative deviation of -0.53%.

It is important to stress that an intense recirculation zone is developed in the vicinity of the divergent wall, right downstream the separation point. An oblique shock is initiated with the formation of a sliding line that splits between the core flow and the backflow (Figs. 9, 10).

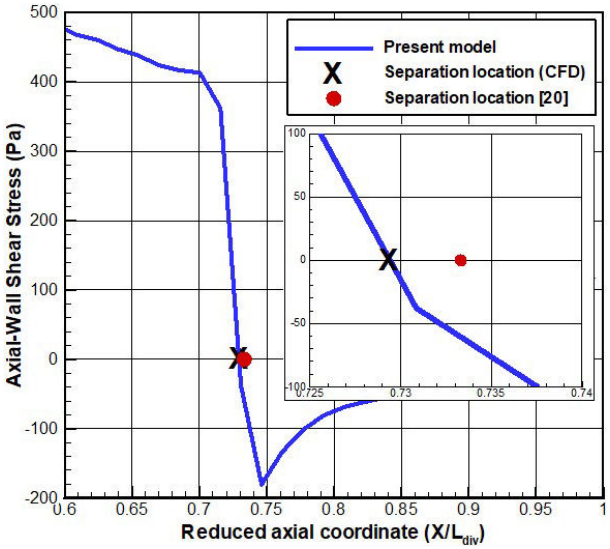

FIGURE 8. Shear stress evolution along the divergent wall.

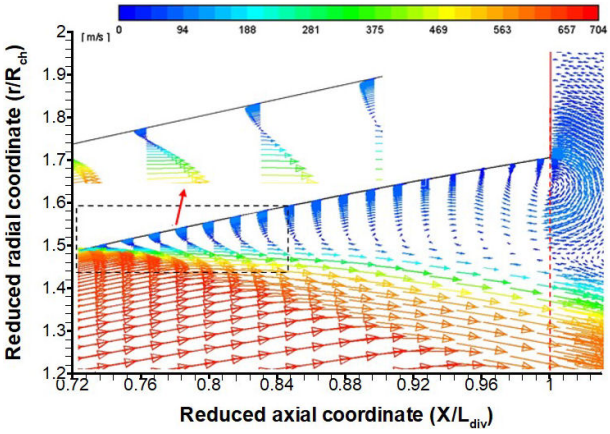

FIGURE 9. Sketch of the flow recirculation in the post-separation zone.

Accordingly, the spatial contour of the Mach number clearly shows the different zones around the separation (Fig. 10).

In comparison with the available experimental data, the numerical values for the Mach number exhibit a good agreement, with a relative deviation less than 1.42% for the oblique shock and less than 0.5% for the reflected shock. The triple point is also accurately recovered, with a relative error of 1.11% compared to the measurements.

With such flow recirculation in the post-separation zone, the exit stream is no longer parallel to the nozzle axis. Consequently, a radial gradient of the exit velocity is noticed, which

TABLE I. Thrust coefficient values for several exit conditions.

cases	Adaptation	Design point [20]	Present model
Thrust coefficient (CF)	1.5701	1.6538	1.0299

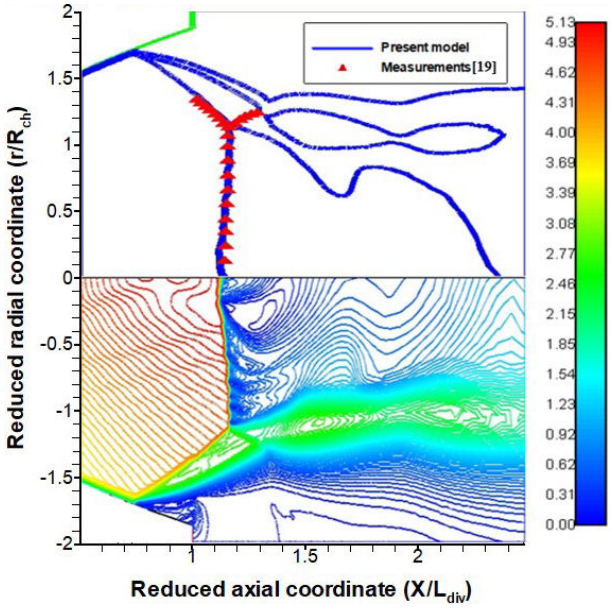

FIGURE 10. Iso-Mach lines around the separation zone.

has the effect of altering the value of the thrust coefficient Table I, in comparison with the adaptation (ideal) case, where the nozzle inflow expands up to a pressure equilibrium state with the far-field flow.

Table I depicts several thrust coefficient values, with regards to the conditions (γ, p_e) at the nozzle exit. In the present model, the thrust coefficient value is obtained from a cell-volume weighting of the heat capacity $(C_{p_{\mathrm{N}_2}})$ and the static pressure (P_e), across the exit section. As it was expected, the adaptation condition highly overestimates the numerical thrust coefficient with a discrepancy with exceeds 34%. It is worthy noticing that an indirect calculation of the "experimental" thrust coefficient was performed, using the design Mach number value, provided by Stark *et al* [20]. The

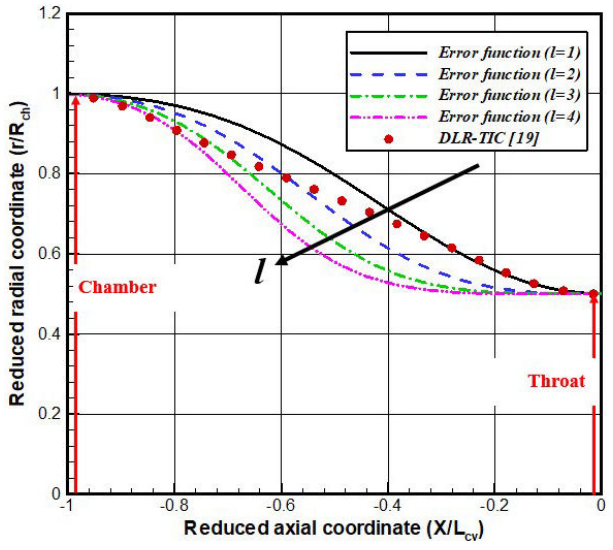

FIGURE 11. Convergent wall profiles for several l values.

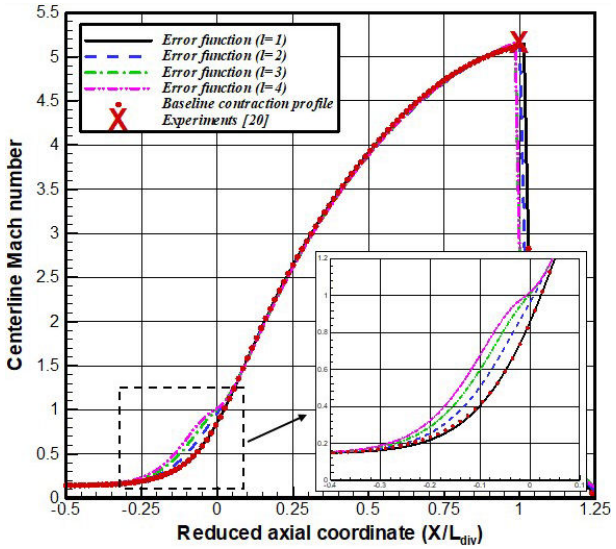

FIGURE 12. Centerline Mach number evolution for several convergent profiles.

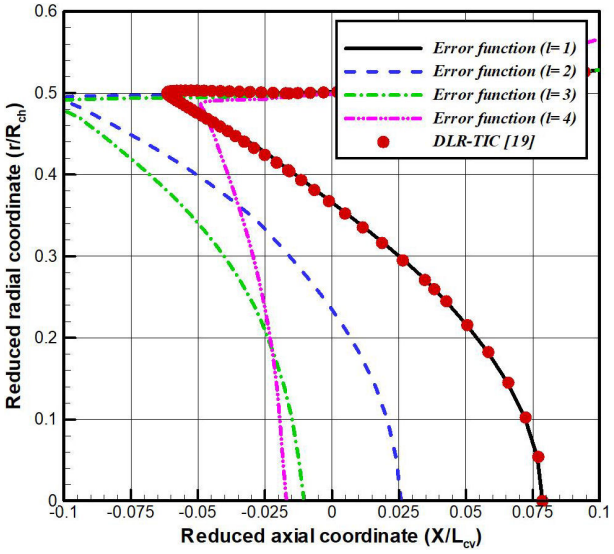

FIGURE 13. Sonic line curves distribution in the throat region.

numerical calculation of the thrust coefficient also underestimates the design value by more than -37%. This tendency was expected, since the provided design Mach number value, was derived under ideal (thermodynamic) flow considerations [20,24,25].

In the following calculations, geometrical variants of the TIC-DLR nozzle will be generated according to the contraction profiles. The baseline data $(D_{\rm ch}, D_{\rm th}, D_e, L_{\rm cv}, L_{\rm div})$ will be replicated from the original geometry and kept unchanged. The convergent shapes will be approximated by a set of Error function profiles (Fig. 11).

It is worthy noticing that the design parameter l is the only factor which controls the flatness of the generated profiles. For high l values, the contraction variants exhibit a strong inflection at the central region, while their flattening at the geometric throat, is highly improved Fig. 11. A sensitivity analysis revealed that curvatures of the convergent variants become nearly identical, for values of the flatness coefficient greater than $l = 5$ [21].

In the convergent part of the nozzle, the use of several variants induces small changes of the centerline Mach number (Fig. 12). Indeed, one notice an increase in the Mach number values as well as the flatness parameter is high, specifically in the throat upstream region. The contraction variant with $l = 1$ coincides perfectly with the baseline (experimental) profile. It is an important to mention note that the profile variant with $l = 4$ recovers exactly a sonic condition (Mach = 1) at the geometrical throat of the nozzle, in contrast to the other variants for which the flow remains subsonic. However, the supersonic core-flow in the divergent part of the nozzle, remains slightly sensitive to the contraction profile variants, with nearly identical exit Mach numbers.

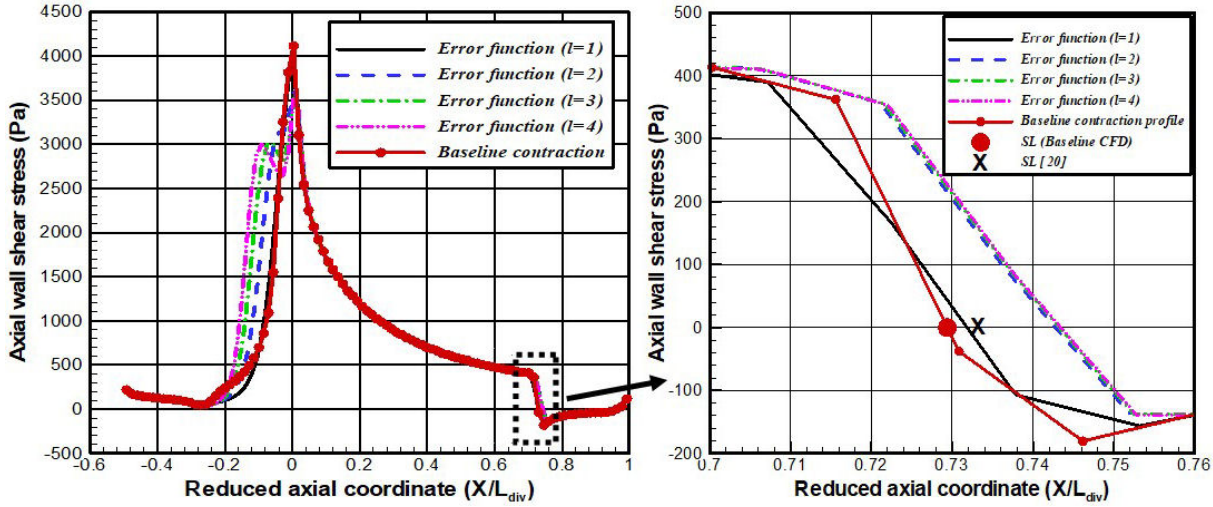

FIGURE 14. Flow separation location (SL) for several contraction profiles.

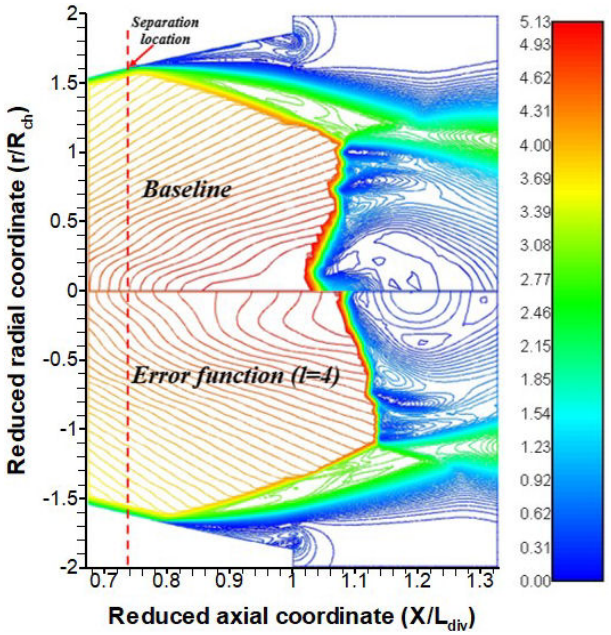

FIGURE 15. Mach number contour (baseline-top & $l = 4$-bottom contraction profiles) near the separation.

Focusing on the throat section, the radial evolution of the Mach = 1 lines is represented in Fig. 13. It is quite clear that the baseline profile as well as the variants with $l = 1$ and $l = 2$ recovers a sonic Mach number $(M = 1)$ on the nozzle axis, downstream of the geometrical throat. Here, the flow in the vicinity of the wall becomes sonic upstream the throat. Consequently, the flow through the throat develops into both subsonic and supersonic slices. In fact, this is not the case for the variants with $l = 3$ and $l = 4$ where the sonic velocity is reached right upstream the throat, into the whole radial slice. The specific case where $l = 4$ remains the most interesting profile in which the sonic line exhibits the most vertical pattern. In the same context, contraction profiles variation has a direct repercussion on the flow separation location (SL) in the divergent part of the nozzle. Hence, Fig. 14 shows the axial shear stress distribution along the nozzle walls and provides the flow separation point, which is still located upstream of the divergent exit section. It is noticed that the separation point moves to the divergent exit direction as well as the profile flatness increases. The variant which corresponds to $l = 4$ exhibits the most important SL, representing therefore a relative displacement of $+1.38\%$, in comparison with the baseline contraction profile.

This behavior is also depicted in spatial contours of the Mach number, for the baseline (top) and the variant $l = 4$ (bottom) contraction profiles (Fig. 15). The figure below clearly shows that both the oblique and normal shocks for the error function profile $(l = 4)$ are located downstream their baseline location.

As the flow separation location moves downstream with the increase of the contraction profile flatness, the core-flow is believed to be an "undisturbed" region of the expanding stream. Consequently, the flow momentum increases as the upstream zone of the separation enlarges, allowing therefore an improvement the nozzle thrust.

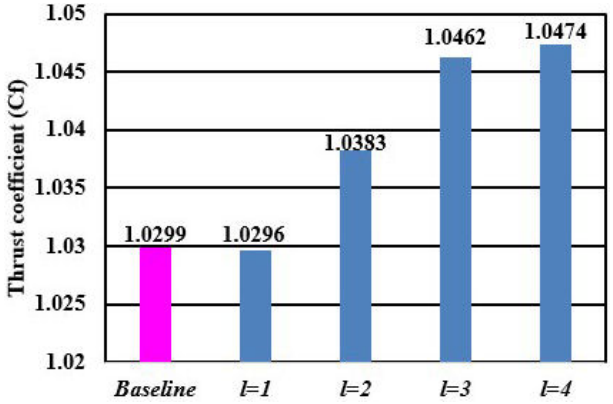

FIGURE 16. Thrust coefficient comparison for several contraction profiles

Figure 16 depicts several thrust coefficient values with regard to separation locations. It is worthy noticing that the profile variant with $l = 1$ provides almost the same thrust as the baseline case. This insignificant discrepancy was expected since this variant exhibits the same patterns for the sonic line and the separation location as the baseline profile. The contraction profile with $l = 4$ shows a relative improvement of $+1.7\%$ on the thrust coefficient, compared to the baseline case. The thrust coefficient is this overexpanded case still remains below its ideal value, obtained for the adaptation exit condition.

6. Conclusion

A set of contraction curves were investigated numerically in the aim to control the shock waves and the separation location in an overexpanded nozzle. In this direction, wall static pressure, separation location, Mach disk and shock structure were validated and compared with the DLR experimental data, provided by the nozzle test-rig.

The main conclusions of this CFD analysis can be drawn as follows:

1. There was a good agreement between numerical results for the baseline case, and the DLR measurements.

2. The flatness of the contraction was more pronounced in the vicinity of the throat, with the increase of the parameter (l).

3. The contraction profile with $l = 4$, was the most interesting specific case, which recovers a quasi- straight sonic line and moved the separation location (SL) towards the exit direction.

4. It was stressed that the contraction profile with $l = 4$ showed a relative improvement of $+1.7\%$ on the thrust coefficient, in comparison to the baseline profile.

Nomenclature

A	Cross sectional area	ν	kinematic viscosity
C_f	Thrust coefficient	τ	Viscous stress tensor
D	diameter	**Subscripts**	
F	nozzle thrust	a	ambient
l	flatness coefficient	ch	chamber
L_{cv}	convergent length	e	exit
L_{div}	divergent length	th	throat
M	Mach number	w	wall
P	static pressure	**Abbreviations**	
R	radius	CFD	computational fluid dynamics
r	Radial coordinate	CV	convergent nozzle
T	static temperature	CV-DV	convergent-divergent nozzle
u_x	axial velocity	DLR	German Aerospace Center
u_r	radial velocity	DV	divergent nozzle
X	axial coordinate	FSS	free shock separation
Y^+	Wall Yplus	MLN	minimum length nozzle
Greek symbols		MOC	method of characteristics
γ	Specific heat ratio	NPR	nozzle pressure ratio
μ	dynamic viscosity	RSS	restricted shock separation
ρ	density	SL	separation location
σ	normal stress tensor	TIC	truncated ideal contoured nozzle

Acknowledgements

The authors would like to acknowledge the financial support of the DGRSDT, the General Direction for Scientific Research and Technological Development, Algeria.

1. S. Gilham, P. Ivey, and J. Owen, The Transfer of heat by Self-induced flow in a rotating tube, *J. Turbomach.* **116** (1994) 316, https://doi.org/10.1115/1.2928367.
2. C. H. Lee, M. Louni, and N. Syred, Centrifuge design for sub-micron particle separation, *Energy R and D* **17** (1995) 51.
3. M. Al-Ajlouni and A. Al-Hamdan, Engine exhaust operated ejector for vehicle air conditioning, *Mutah Journal for Research and Studies* **17** (2002) 119.
4. E. Martelli *et al*., Flow dynamics and wall-pressure signatures in a high-Reynolds-number overexpanded nozzle with free shock separation, *Journal of Fluid Mechanics* **895** (2020) A29, https://doi.org/10.1017/jfm.2020.280.
5. P. Caisso *et al*., A liquid propulsion panorama, *Acta Astronautica* **65** (2009) 1723.
6. G. Daviller *et al*., Prediction of Flow Separation and Side-loads in Rocket Nozzle Using Large-eddy Simulation, International *Journal of Computational Fluid Dynamics* **34** (2020) 622, https://doi.org/10.1080/10618562.2020.1786540.
7. A. Hadjadj, Y. Perrot, and S. Verma, Numerical study of shock/boundary layer interaction in supersonic overexpanded nozzles, *Aerospace science and technology* **42** (2015) 158, https://doi.org/10.1016/j.ast.2015.01.010.
8. J. C. Restrepo, A. F. Bolaños-Acosta, and J. R. Simões- Moreira, Short nozzles design for real gas supersonic flow using the method of characteristics, *Applied Thermal Engineering* **207** (2022) 118063, https://doi.org/10.1016/j.applthermaleng.2022.118063.
9. B. M. Argrow and G. Emanuel, Computational analysis of the transonic flow field of two-dimensional minimum length nozzles, *J. Fluids Eng.* **113** (1991) 479.
10. J. Oštlund and B. Muhammad-Klingmann, Supersonic flow separation with application to rocket engine nozzles, *Appl. Mech. Rev.* **58** (2005) 143, https://doi.org/10.1115/1.1894402.
11. R. Stark, Flow separation in rocket nozzles, a simple criteria, In 41st AIAA/ASME/SAE/ASEE Joint Propulsion Conference & Exhibit (2005) p. 3940, https://doi.org/10.2514/6.2005-3940.

12. R. Cuffel, L. Back, and P. F. Massier, Transonic flowfield in a supersonic nozzle with small throat radius of curvature., *AIAA Journal* **7** (1969) 1364, https://doi.org/10.2514/3.5349.

13. T.-L. Ho and G. Emanuel, Design of a nozzle contraction for uniform sonic throat flow, *AIAA journal* **38** (2000) 720, https://doi.org/10.2514/2.1019.

14. D. Brassard and M. Ferchichi, Transformation of a polynomial for a contraction wall profile, *J. Fluids Eng.* **127** (2005) 183, https://doi.org/10.1115/1.1852492.

15. E. M. Germer and C. H. Marchi, Effect of Convergent Section Contour on the Sonic Line in Rocket Engine Nozzles, *J Aerosp Technol Mana* **10** (2018) e3218, https://doi.org/10.5028/jatm.v10.924.

16. M. Kumar, R. Sahoo, and S. Behera, Design and numerical investigation to visualize the fluid flow and thermal characteristics of non-axisymmetric convergent nozzle, *Engineering Science and Technology, an International Journal* **22** (2019) 294, https://doi.org/10.1016/j.jestch.2018.10.006.

17. H. Tian *et al*., Numerical and experimental investigation of throttleable hybrid rocket motor with aerospike nozzle, *Aerospace Science and Technology* **106** (2020) 105983, https://doi.org/10.1016/j.ast.2020.105983.

18. H. Kronmüller *et al*., Cold gas subscale test facility p6. 2 at dlr lampoldshausen, In International Symposium on Propulsion for Space Transportation of the XXIst century (Palais des Congress, Versailles, France, 2002) pp. 1-8, https://elib.dlr.de/1561/.

19. R. Stark and G. Hagemann, Current status of numerical flow prediction for separated nozzle flows, In 2nd European conference for aerospace sciences (EUCASS), (Brussels (Belgium)2007) https://elib.dlr.de/49262/.

20. R. Stark and B. Wagner, Experimental study of boundary layer separation in truncated ideal contour nozzles, *Shock Waves* **19** (2009) 185, https://doi.org/10.1007/s00193-008-0174-6.

21. M. Nedjari, E. Mahfoudi, and A. Benarous, Prediction numérique du coefficient de poussé pour une tuyere surdetendue, In Third International Conference on Energy, Materials, Applied Energetics and Pollution ICEMAEP2016 (Université des Frères Mentouri Constantine, Constantine, Algeria, 2016) p. 195, http://hdl.handle.net/123456789/132965.

22. M. Nedjari, A. Benarous, and A. Benazza, Analyse du décollement libre dans une tuyère sur-détendue: Effet des paramètres de conception, *In Mechanical French Congress (CFM)*, (Brest, France2019).

23. X. He, F. Zhao, and M. Vahdati, A Turbo-Oriented Data-Driven Modification to the Spalart-Allmaras Turbulence Model, *ASME J Turbo*, (in press) (2022) 80456.

24. P. L. Roe, Characteristic-based schemes for the Euler equations, *Annual review of fluid mechanics* **18** (1986) 337, https://doi.org/10.1146/annurev.fl.18.010186.002005.

25. S. A. Khan *et al*., Investigation of the effects of nozzle exit mach number and nozzle pressure ratio on axisymmetric flow through suddenly expanded nozzles, *International Journal of Engineering and Advanced Technology (IJEAT) ISSN* **8** (2019) 570.